H$_2$ Evolution over g-C$_3$N$_4$/Cs$_x$WO$_3$ under NIR light

Anye Shi[a], Huihui Li[a,*], Shu Yin[b], Jiachi Zhang[a,*], Yuhua Wang[a]

[a] National & Local Joint Engineering Laboratory for Optical Conversion Materials and Technology, School of Physical Science and Technology, Lanzhou University, 222 South Tianshui Road, Lanzhou 730000, PR China
[b] Institute of Multidisciplinary Research for Advanced Materials, Tohoku University, 2-1-1 Katahira, Aoba-ku, Sendai 980-8577, Japan

ARTICLE INFO

ABSTRACT

Single layer g-C$_3$N$_4$ and nanorod Cs$_x$WO$_3$ are coupled to form a composite photocatalyst. During a simple method, no destruction has occurred and the optimal mass ratio of g-C$_3$N$_4$ is 80% as evidenced by systematic analyses. In comparison to pure g-C$_3$N$_4$ and Cs$_x$WO$_3$, the composite exhibits significantly high photocatalytic and photoelectrochemical activity for H2 evolution and RhB/phenol degradation under UV, visible and NIR light irradiation. The enhanced photoactivities are attributed to the strong synergistic effect between the localized surface plasmon resonance (LSPR) and the heterojunction interface sensitization, which results in the improvement of charge carriers generation and separation in the composite.

1. Introduction

Conjugated g-C$_3$N$_4$ photocatalysts with delocalized π system have attracted much attention due to the fast separation and the slow recombination of photo-generated electrons and holes [1]. Combination of g-C$_3$N$_4$ with a proper semiconductor could be expected to keep the conjugated system and improve the photocatalytic activity in an extended spectral range [2–6]. Different semiconductors have been chosen to hybridize g-C$_3$N$_4$ as efficient photocatalysts and successfully exhibit the stability, such as using CdZnS, ZrS$_2$ and nitrogen-doped TiO$_2$ [7–9].

Thanks to their proper band structures, some tungsten semiconductors exhibit positive effects on the photocatalysis efficiency of composites including WO$_3$/g-C$_3$N$_4$, RuO$_2$/PtO$_x$/WO$_3$ and metal/WO$_{2.72}$/rGO [10–12]. In addition, it is found that vacancy-rich tungsten oxide materials, such as WO$_{2.72}$, Na$_{0.75}$WO$_3$, and M$_{0.33}$WO$_3$ (M = Na, Cs, Tl, Rb), have strong NIR absorption due to the generation of localized surface plasmonic resonance (LSPR) [12–15]. Previous works have demonstrated that LSPR materials can enhance optical absorption and generation of charge carriers as a photosensitizer [12–20]. Cs$_x$WO$_3$, a new LSPR material, has special W^{5+}, oxygen vacancies and free electrons to form localized states just below its conduction band, which will has a benefit for charge transfer [21]. Therefore, Cs$_x$WO$_3$ appears to be a suitable candidate for photocatalysis with a unique property of IR absorption and favorable conductivity [21–24].

The combination of g-C$_3$N$_4$ and Cs$_x$WO$_3$ is expected to be a potential ideal system with efficient charge separation and transfer for full-spectrum responsive catalytic reactions. In this work, it reports for the first time that protonated single layer g-C$_3$N$_4$ and nanosized Cs$_x$WO$_3$ were selected to form a composite for photocatalysis and photoelectrochemical reaction. The fabrication of the g-C$_3$N$_4$/Cs$_x$WO$_3$ composite was carried out by an electrostatic attraction method. With the systematical investigation of photocatalytic performance and photoelectrochemical activity, the results suggest that the combination of g-C$_3$N$_4$ and Cs$_x$WO$_3$ can effectively enhance both the UV–vis light and NIR photocatalytic activity. In addition, the photocurrent of composite is greatly enhanced under both visible light and NIR irradiation. The possible mechanism in the reaction process and the synergic effect between g-C$_3$N$_4$ and Cs$_x$WO$_3$ were also investigated.

2. Experimental section

2.1. Samples preparation

Melamine was used as a starting material. WCl$_6$ and CsOH·H$_2$O were used as a tungsten and a caesium source respectively. All chemicals were purchased from Aladdin Chemical Reagent Co., Ltd. and used as received without further purification.

Single layer g-C$_3$N$_4$ was prepared by the protonation treatment of bulk g-C$_3$N$_4$ from the thermal polycondensation of melamine [25]. First, melamine (1.60 g) was heated at 550 °C for 3 h. Then, bulk one (1 g) was dispersed in HCl (5 mL, 37%) for 24 h. After centrifugation, washing and drying, the final single layer g-C$_3$N$_4$ particles were obtained.

Nanosized Cs$_x$WO$_3$ was prepared by a solvothermal process [23]. WCl$_6$ ethanol solution and CsOH ethanol solution were mixed with a
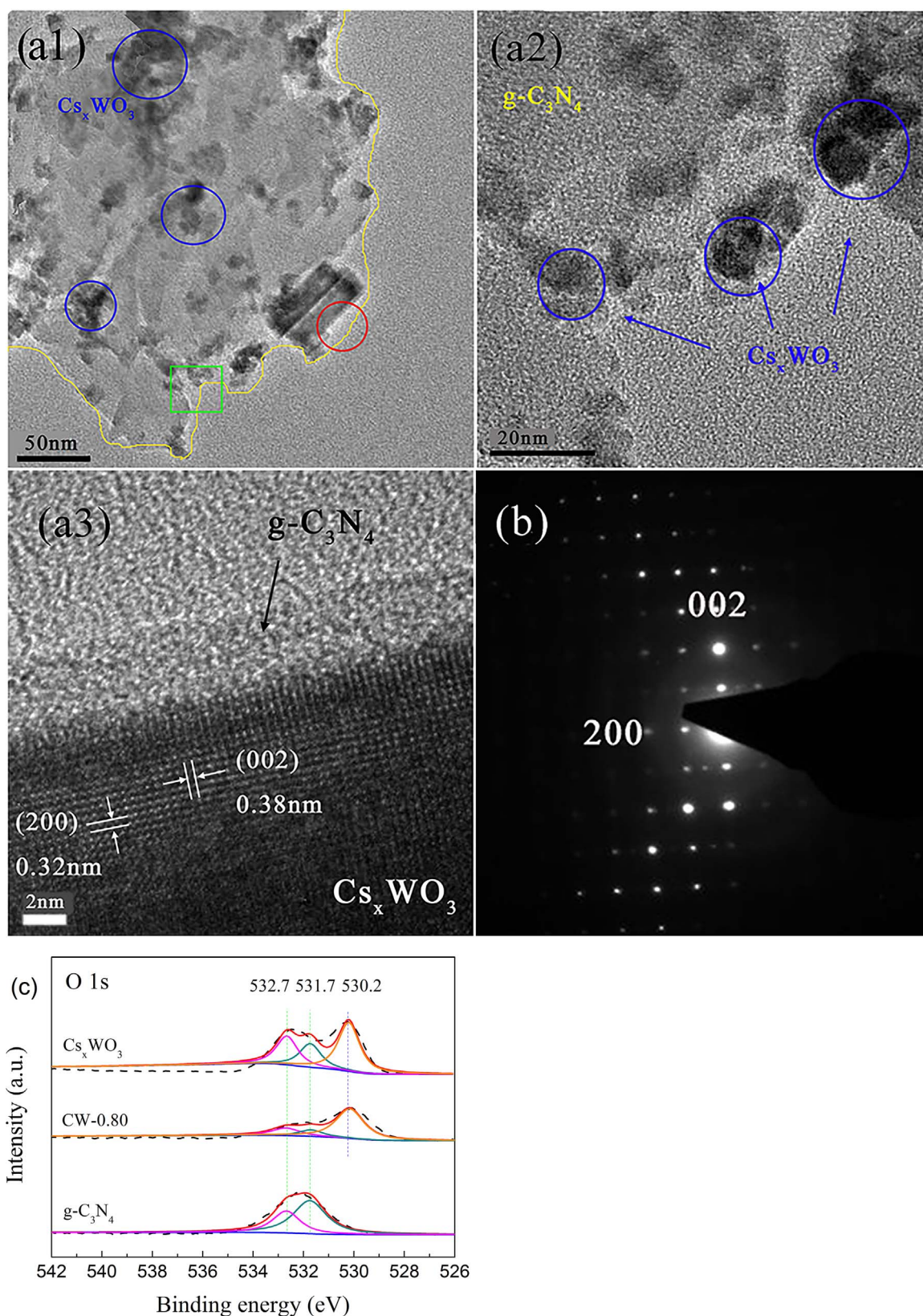
Fig. 1. (a1,a2) TEM, (a3) HRTEM images, and (b) SAED pattern of CW-0.80 composite; (c) high-resolution O1s XPS of g-C$_3$N$_4$, Cs$_x$WO$_3$ and CW-0.80.

nominal Cs/W atomic ratio of 0.5 to form precursor solution. Then, after the solvothermal reaction, the final Cs$_x$WO$_3$ was obtained after centrifugation, washing and drying.

According to the differences in the surface electrical behavior of

protonated g-C$_3$N$_4$ and Cs$_x$WO$_3$, it is easy to fabricate a uniform hybrid by electrostatic attraction in aqueous solution [21,25]. Typically, Cs$_x$WO$_3$ (0.5 g) and a designed amount of as-prepared single layer g-C$_3$N$_4$ were added into deionized water (100 mL) and then treated by

Table 1
Physical properties of g-C$_3$N$_4$, Cs$_x$WO$_3$ and CW-0.80.

Samples		g-C$_3$N$_4$	Cs$_x$WO$_3$	CW-0.80
Elemental analysis (%)	C	40.69	–	22.65
	N	50.63	–	28.14
	O	8.68	17.26	12.61
	Cs	–	15.94	7.00
	W	–	66.80	29.60
Specific surface area (m^2/g)		37.6	32.5	35.7
Average particle size (nm)		308	177	332

ultrasonication for 4 h. The powder product was separated by centrifugation, and then vacuum dried at 60 °C overnight. The as-prepared composites are named as CW-y (y = 50%, 67%, 75%, 80%, 83%), where y refers to the g-C$_3$N$_4$ weight percents in the composite.

2.2. Characterization

X-ray diffraction (XRD) characterizations were performed on a Shimadzu XRD-6000 powder X-ray diffractometer with CuKα radiation. Fourier transform infrared (FT-IR) spectra were recorded using a VERTEX 70 V/80 V spectrometer (Bruker, Germany) by means of the KBr pellet technique. The UV–vis diffuse reflectance spectra (DRS) were obtained on a Perkin-Elmer Lambda 950 spectrometer equipped with Labsphere integrating over the spectral range of 250–1600 nm. Transmission electron microscopy (TEM) and high-resolution TEM (HRTEM) images were obtained with a JEOL JEM-2100 microscope at 200 kV. The photoluminescence (PL) spectra were obtained on an FLS-920T fluorescence spectrophotometer. The specific surface areas were measured out by the BET method (Micromeritics Instrumetns, TriStar α3020). X-ray photoelectron spectroscopy (XPS) measurement was done using a Kratos AXIS Ultra DLD XPS system with a monochromatic AlKα source and a charge neutralizer, all the binding energies were referenced to the C1s peak at 284.6 eV of the surface adventitious carbon. The particle size distribution was analyzed in water solution via Dynamic light scattering measurement (DLS) with a BI-200SM laser light scattering instrument. The transient absorption spectra (TAS) were obtained with an Edinburgh LP920 specteophotometer. The OPO laser (Opolette HE 355 LD UVDM, Optotek Inc.) with output wavelength of 236–2400 nm was used as the excitation source. All of the samples were purged with nitrogen to evacuate oxygen before evaluation. A Vario EL cube was employed to carry out elementary analysis and an IRIS ER/S was used to determine element content via inductively coupled plasma atomic emission spectroscopy (ICP-AES).

2.3. Photocatalytic activities test

Six different lamps have been used as a light source respectively, with details as follows.

(A) a compositive LED lamp (365–940 nm, CEL-LAB100E, CEAULIGHT) with 100.7 mW/cm^2 intensity.
(B) a white LED lamp (400–750 nm) with 9.4 mW/cm^2 intensity.
(C) a monochrome red LED lamp (660 nm) with 10.1 mW/cm^2 intensity.
(D) a monochrome blue LED lamp (460 nm) with 2.5 mW/cm^2 intensity.
(E) a monochrome UV LED lamp (360 nm) with 0.4 mW/cm^2 intensity.
(F) a 980 nm laser lamp (500 mW).

H$_2$ generation experiment: Typically, the as-prepared sample (50 mg) was dispersed in an aqueous solution (100 mL) containing triethylamine (TEOA, 10 mL, 10 vol.%) as a sacrificial agent. Pt (3 wt. %) was loaded on the surface of the photocatalyst as a cocatalyst by the photodeposition of H$_2$PtCl$_6$. Prior to irradiation, the reaction solution

was sealed by a silicone stopper, and subsequently flushed with dry nitrogen to remove air, and sonicated for ~1–2 min in dark to guarantee an adsorption-desorption equilibrium between the photocatalyst and reactant. A calibrated Varian GC-3380 Gas Chromatograph equipped with a thermal conductivity detector was employed to determine the evolved hydrogen, using nitrogen as the carrier gas.

Total water splitting: The test was performed under the same condition as that in hydrogen production but no sacrificial agent.

Photocatalytic degradation: The photocatalytic degradation activities were evaluated by the decomposition of Rhodamine B (RhB, 10 mg/L) under visible light or NIR irradiation. The photodegradation reactions were carried out with pollutant solution (50 mL) and photocatalysts (25 mg). After reaching adsorption-desorption equilibrium in the dark for 2 h, the stirred solutions were irradiated by visible light or NIR light. At every time intervals, the solutions were centrifugated and monitored by the UV–vis spectraphotometer.

2.4. Determination of reactive species

To investigate the active species responsible for the photocatalytic degradation, various scavengers, including isopropyl (i-PrOH, IPA, 1.31 mmol/L), ammonium oxalate (AO, 0.81 mmol/L), benzoquinone (BQ, 0.93 mmol/L) were respectively introduced into the solution of RhB. To detect generation of reactive species, electron paramagnetic resonance (EPR) signals of radicals spin-trapped by 5, 5-dimethyl-1-pyrroline-N-oxide (DMPO) were collected by a Bruker A300-9.5/12 at 100 kHz field modulation in the standard TE102 regular cavity operating in the X-band at 9.45 GHz.

2.5. Photoelectrochemical and electrochemical measurement

CHI 660b electrochemical workstation (Shanghai Chenhua) was applied for the electrochemical measurements.

Photocatalytic (PC), Photoelectrochemical (PEC) and electronchemical (EC) degradation experiments: The evaluations were carried out in a glass reactor. The degradation target was phenol (25 mL, 5 mg/L). A 0.1M Na$_2$SO$_4$ solution was used as the electrolyte.

The electrochemical impedance spectroscopy (EIS): It was measured at −1.4 V (vs. RHE), and the perturbation signal was 5 mV with the frequency ranged from 0.1 Hz to 100 kHz.

Transient photocurrent measurement: Photocurrents were measured using an electrochemical analyzer (CHI 660b) in a standard three-electrode system using the prepared samples as the working electrodes with an active area of ca. 1.00 cm × 1.00 cm, a Pt foil and an Ag/AgCl (saturated KCl) electrode were used as the counter electrode and reference electrode, respectively. A 0.1M Na$_2$SO$_4$ solution was used as the electrolyte. A 500 W Xe lamp with intensity of 43 mW cm^{-2} was served as a visible light source. Working electrodes were prepared according to our previous work [9].

3. Results and discussion

3.1. Structural and morphological characterization

The structure of CW composites was first characterized by XRD and FT-IR. As shown in Fig. S1a, only the (002) peak at 27.4° (JCPDS No. 871526) is observed in pure g-C$_3$N$_4$. The restacking of nanolayer along (001) direction caused the disappearance of the (100) peak at 13.0° of such g-C$_3$N$_4$ [25,26]. The XRD pattern of Cs$_x$WO$_3$ exhibits pure hexagonal tungsten bronze structure without any other impurity peaks (JCPSD No. 831334). After coupling, the characteristic peaks belonged to Cs$_x$WO$_3$ are all presented in the XRD patterns of all composites. The (002) peak of g-C$_3$N$_4$ should be overlapped by the peak at ~27.4° of Cs$_x$WO$_3$. To further investigate the connecting mode between g-C$_3$N$_4$ and Cs$_x$WO$_3$ in the CW compound, FT-IR and XPS characterizations of pure g-C$_3$N$_4$, Cs$_x$WO$_3$ and CW samples were carried out. As shown in
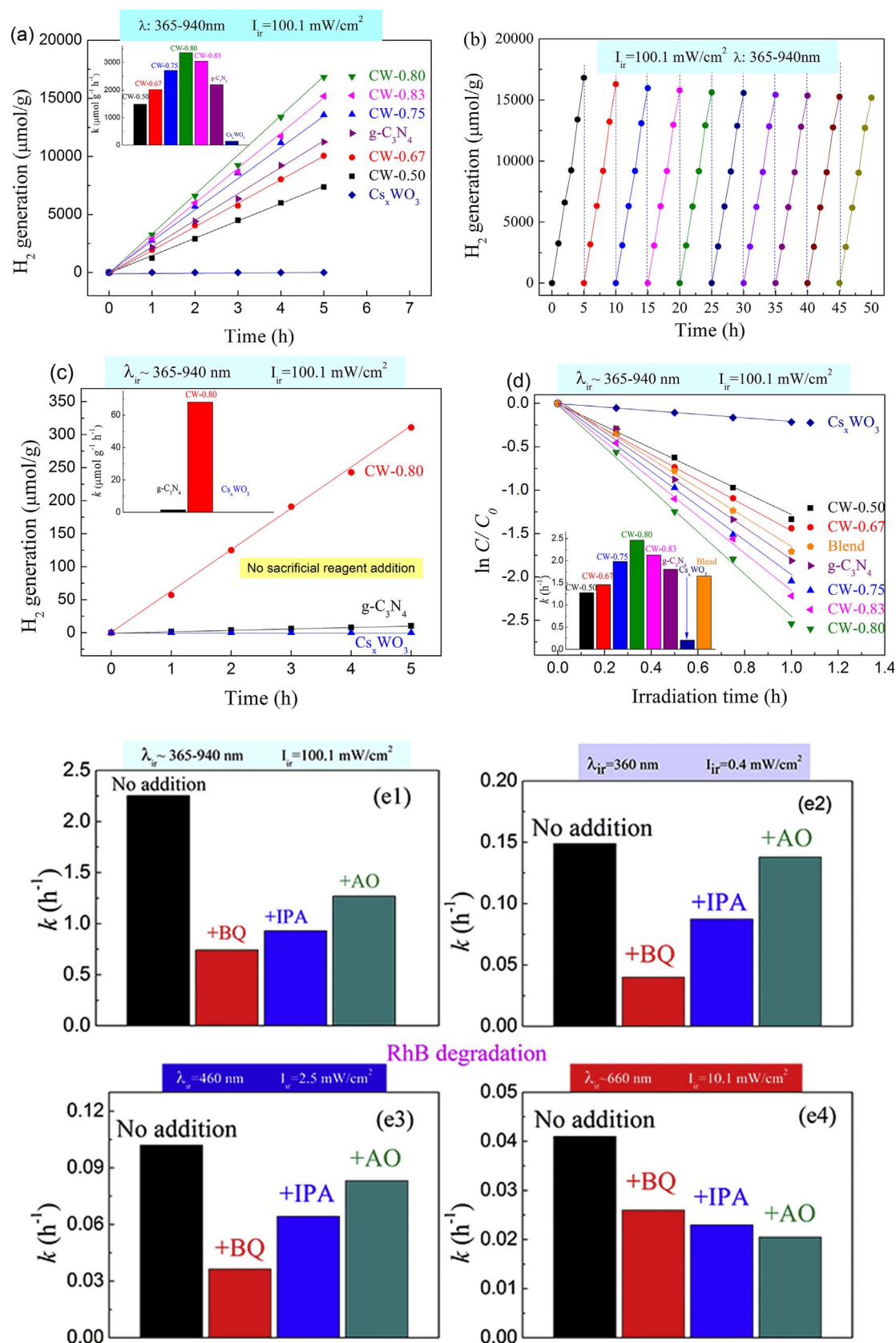
Fig. 2. (a) H$_2$ production of g-C$_3$N$_4$, Cs$_x$WO$_3$ and CW photocatalysts and (b) stability test of H$_2$ production for CW-0.80 using TEOA as the sacrificial agent; (c) H$_2$ production of g-C$_3$N$_4$, Cs$_x$WO$_3$ and CW-0.80 without any sacrificial agent; (d) photocatalytic RhB degradation over g-C$_3$N$_4$, Cs$_x$WO$_3$ and CW photocatalysts. (a–d) The reactions were carried out under full-spectrum light (365–940 nm) irradiation. (e) The photoinduced carriers trapping in the system of photocatalytic RhB degradation over CW-0.80 by adding different active radical captures under different light irradiation; (f) DMPO spin-trapping EPR spectra of CW-0.80 methanol dispersion for DMPO-·O$_2^-$ after different light irradiation (1: DMPO-·O$_2^-$, 2: nitroxide-like radical). (For interpretation of the references to colour in text, the reader is referred to the web version of this article).
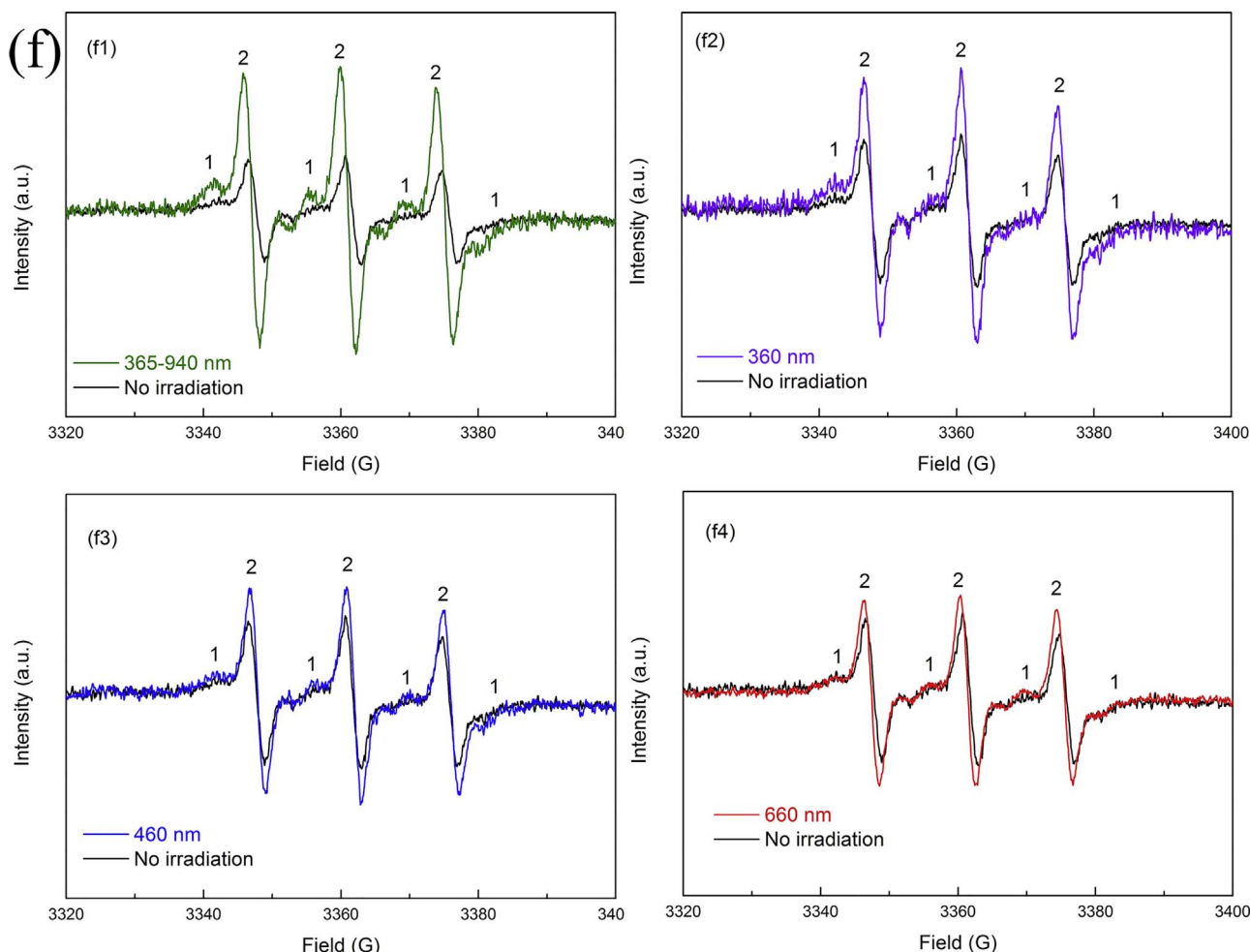
Fig. 2. (continued)

the FT-IR spectra (Fig. S1b), pure g-C_3N_4 has a little stronger IR response than Cs_xWO_3. The peaks at 673 and 969 cm^{-1} are ascribed to the stretching vibrations of W−OW bond and W=O bond respectively, while the broad bands between 550 and 1000 cm^{-1} are attributed to the framework vibrations of Cs_xWO_3 [27,28]. No obvious difference has been observed between pure g-C_3N_4 or Cs_xWO_3 and CW composites except one peak. The new peak at 1054 cm^{-1} in g-C_3N_4/Cs_xWO_3 compounds can be attributed to the W−N bond, indicating the connection formed in the g-C_3N_4/Cs_xWO_3 compounds [29].

Fig. S1c1 shows two peaks, one is the standard C-C peak at 284.7 eV, while another one can be fitted into sp^2 and sp^3 C. However, compared with g-C_3N_4, the peak composed of sp^2 and sp^3 C shifts to higher binding energy at 288.5 eV in CW-0.80, indicating the formation of W−C and/or C−O−W [30]. As shown in the N 1s spectra (Fig. S1c2), the peak at 398.8 eV in g-C_3N_4 can be attributed to anionic N−, while that shifts to 399.1 eV in CW-0.80 [31]. To form the CW composite, O ion in O−W−O will be replaced by N. However, N possesses lower electro negativity than oxygen, resulting in the electron density reduction after the composite formation [31]. Therefore, the peak will shift to 399.1 eV in the CW-0.80 [32,33]. In the W 4f spectra (Fig. S1c3), CW-0.80 has two peaks at 37.40 and 35.20 eV, lower than 37.65 and 35.55 eV in Cs_xWO_3. It can also be attributed to the substitution of O^{2-} by N^{3-} and the formation of O−W−N bond [34]. Thus, it can be concluded that g-C_3N_4 coupled with Cs_xWO_3 by N−W−O, C−W−O and W−O−N formation.

Fig. 1a,b show the structure of the CW-0.80 sample obtained through an electrostatic attraction in aqueous solution, characterized by TEM and HRTEM. In Fig. 1a1 and a2, the g-C_3N_4 well exhibits the sheet-like morphology, while some particles are dispersed on the g-C_3N_4. The particle materials should be Cs_xWO_3 [23]. As presented in HRTEM and SAED images (Fig. 1a3 and b), the nanoparticles show continuous and ordered lattice fringes with the lattice spacing of 3.2 Å and 3.8 Å and the crystal plane angle of 90°, which correspond to the (200) and (002) planes, respectively, according to the lattice parameters of hexagonal Cs_xWO_3 [35]. On account of the sheet-like morphology, it can be deduced that the g-C_3N_4 nanosheets are mostly constituted by (002) faces. To further evaluate the combination of g-C_3N_4 and Cs_xWO_3, element map is carried out as shown in Fig. S1e1 and S1e2, which indicates that Cs_xWO_3 is closely contacted with g-C_3N_4.

ICP-AES was used to determine the contents of different elements in the pure g-C_3N_4, Cs_xWO_3 and CW-0.80. As shown in Table 1, the mass contents of C and N are 40.69% and 50.63% in pure g-C_3N_4 and 22.65% and 28.14% in CW-0.80 respectively. The contents of Cs and W are 7.00% and 29.60% in CW-0.80, while 15.94% and 66.81% in pure Cs_xWO_3. The atom ratio of Cs to W and C to N in CW-0.80 are the same as those in pure g-C_3N_4 and Cs_xWO_3. The ICP results are in good agreement with the results of XRD and TEM, further revealing that g-C_3N_4 and Cs_xWO_3 coupled successfully. In addition, the C/N mole ratio of as-prepared g-C_3N_4 is 0.94, which is higher than the theoretical value (0.75). Many investigations also reported the same results, for example, the C/N molar ratio was 0.94 in C. Zhou's work and 0.86 in F. Dong's work [36,37]. C. Dong et al. obtained the g-C_3N_4 sample with the C/N ratio of 0.99 after the same HCl treatment [38]. L.-F. Gao's group reported the C/N molar ratio of their sample was as high as 2.75 after using the hydrothermal method followed by liquid exfoliation [39]. The high level of C/N molar ratio in the g-C_3N_4 samples may be caused by

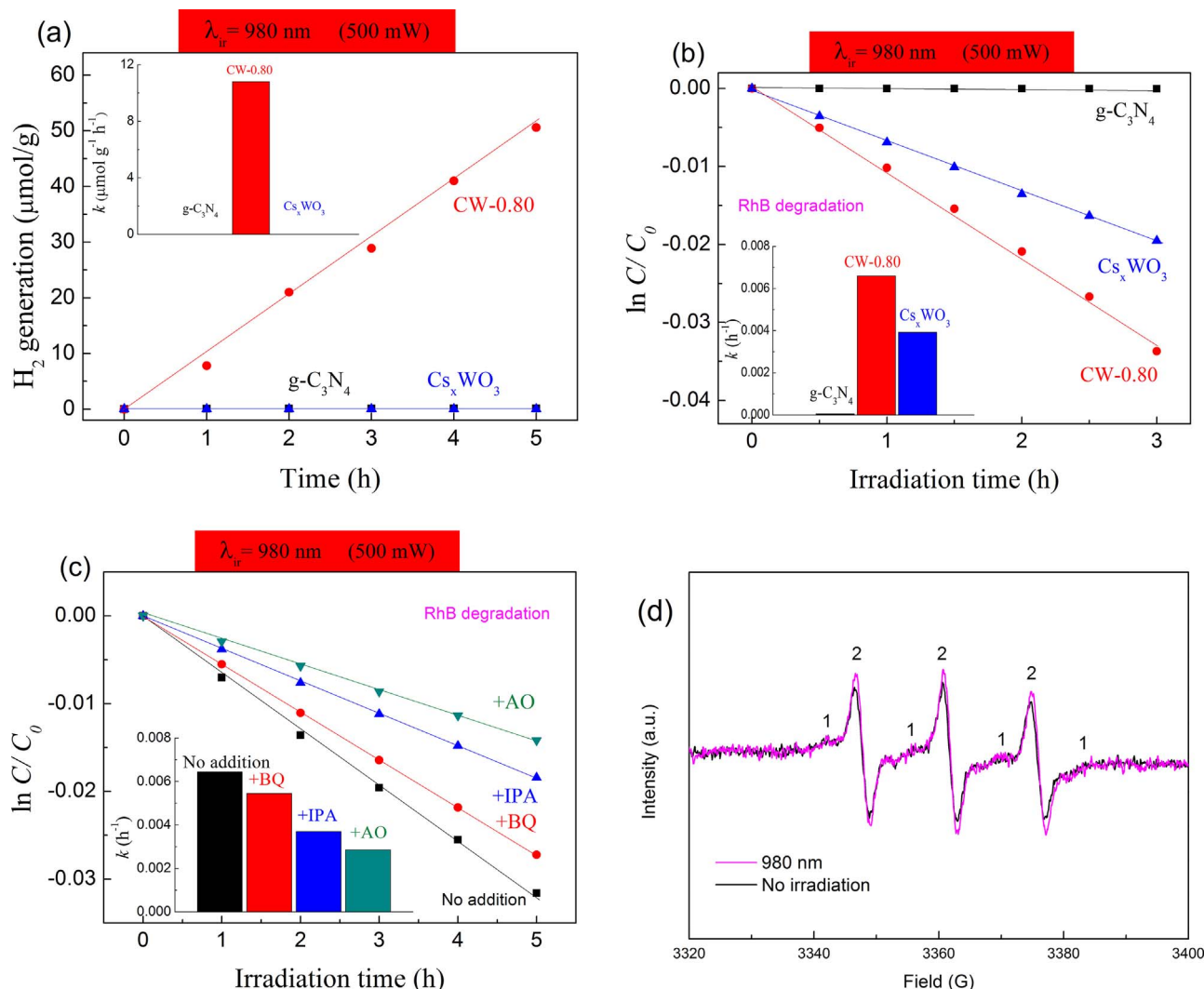**Fig. 3.** (a) H$_2$ production and (b) RhB degradation over g-C$_3$N$_4$, Cs$_x$WO$_3$ and CW-0.80 under NIR light (980 nm) irradiation; (c) The photoinduced carriers trapping in the system of photocatalytic RhB degradation over CW-0.80 by adding different active radical captures under NIR light irradiation; (d) DMPO spin-trapping EPR spectra of CW-0.80 methanol dispersion for DMPO-·O$_2^-$ after NIR light irradiation (1: DMPO-·O$_2^-$, 2: nitroxide-like radical).

the presence of structure defect and surface nitrogen atom loss [40].

Fig. 1c shows the high-resolution XPS of g-C$_3$N$_4$, Cs$_x$WO$_3$ and CW-0.80 calibrated with the reference carbon at 284.6 eV. For the pristine g-C$_3$N$_4$, the O1s peak at 531.7 and 532.7 eV is attributed to the presence of hydroxyl groups [41]. For the pristine Cs$_x$WO$_3$, the main O1s signal consists of three main peaks at binding energies of 530.2, 531.7 and 532.7 eV assigned to O element and hydroxyl groups, respectively [42]. The CW-0.80 composite also exhibits three O1s peaks at 530.2, 531.7 and 532.7 eV. No impurity peak is observed in the O1s spectrum of CW-0.80 composite. All things are in the same situation in the C1s, N1s, W4f, and survey XPS as shown in Fig. S1c1–c4. After hybridization, no serious destruction occurs in the aspect of structure and composition.

In addition, the thickness and morphology of g-C$_3$N$_4$ was confirmed by AFM and TEM analysis. As shown in Fig. S1d1–3, the randomly measured nanosheets are of the thickness from ca. 0.45 nm to ca. 0.91 nm, indicating the exfoliated nanosheets are composed of only one or two stack layers. The TEM image of the g-C$_3$N$_4$ product after exfoliation as presented in Fig. S1d4 displayed layer structure.

3.2. Enhancement of photocatalytic H$_2$ evolution and degradation in UV, visible and NIR light region

Fig. 2a–d shows the photocatalytic activities of g-C$_3$N$_4$, Cs$_x$WO$_3$ and

CW photocatalysts under a compositive LED lamp (365–940 nm) irradiation.

The g-C$_3$N$_4$, Cs$_x$WO$_3$ and CW photocatalysts were first evaluated by the photocatalytic hydrogen evolution under full-spectrum light irradiation. As shown in Fig. 2a, pure Cs$_x$WO$_3$ has hardly any photocatalytic H$_2$ evolution activity. However, after hybridization, the H$_2$ evolution ability is evidently enhanced. All CW composites show much higher photocatalytic H$_2$ evolution activity than pure Cs$_x$WO$_3$ even better than g-C$_3$N$_4$. The CW-0.80 photocatalyst could make 16,806 μmol/g of H$_2$ after 5 h photocatalytic reaction, while the H$_2$ evolution amount is 11,221 μmol/g over g-C$_3$N$_4$. The determined rate constant k of CW-0.80 is 3361 μmol g^{-1} h^{-1} almost 1.5 times as that of pure g-C$_3$N$_4$ (2244 μmol g^{-1} h^{-1}) and 23 times pure Cs$_x$WO$_3$ (146 μmol g^{-1} h^{-1}). It is of particular note that in ten consecutive reactions, the H$_2$ evolution increases steadily as the irradiation time increases with slight fluctuations (Fig. 2b).

To investigate the superiority of CW-0.80, the water splitting performance was determined in pure water without any sacrificial reagents under the same condition. Under full-spectrum light irradiation, in Fig. 2c, the H$_2$ production is obtained of 312.5 and 7.4 μmol/g for CW-0.80 and g-C$_3$N$_4$, respectively. CW-0.80 exhibits an excellent photocatalytic water splitting ability 43 times as high as that of pure g-C$_3$N$_4$, while pure Cs$_x$WO$_3$ has hardly any activity again. The determined rate
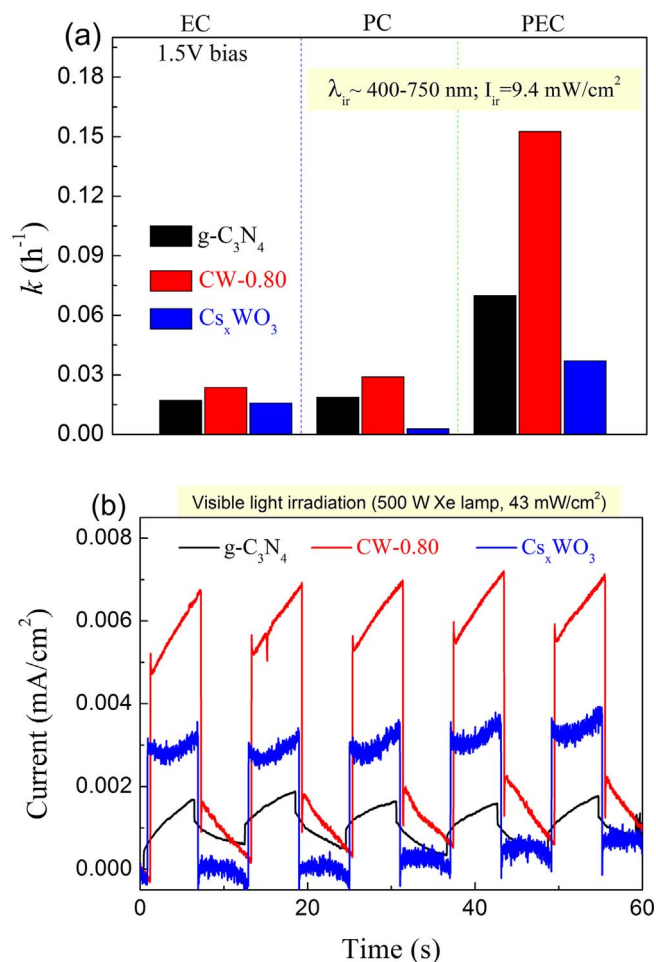
Fig. 4. (a) Electrocatalytic, photocatalytic and photoelectrocatalytic degradation of phenol on g-C$_3$N$_4$, Cs$_x$WO$_3$ and CW-0.80 under visible light (400–750 nm) irradiation; (b) Photocurrent measurements under visible light irradiation of g-C$_3$N$_4$, Cs$_x$WO$_3$ and CW-0.80 film electrodes in 0.1M Na$_2$SO$_4$ aqueous solution.
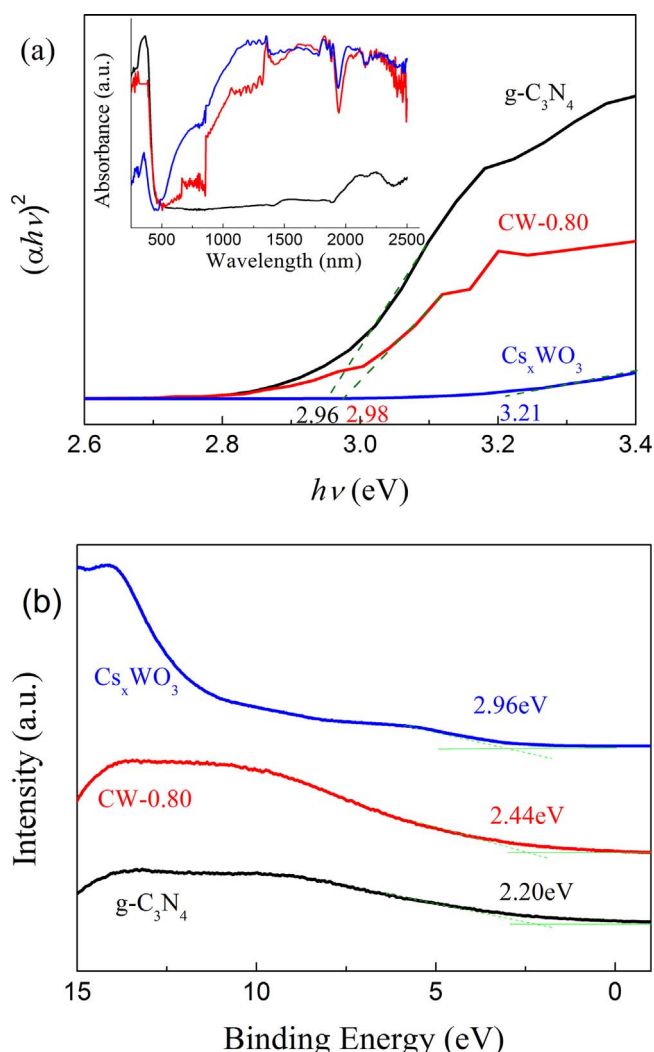

Fig. 5. (a) UV–vis DRS (insert one) and $(\alpha h\nu)^2$ as a function of photon energy ($h\nu$), where α is the Kubelka-Munk function; (b) High-resolution valence band XPS spectra of g-C$_3$N$_4$, Cs$_x$WO$_3$ and CW-0.80. (For interpretation of the references to colour in text, the reader is referred to the web version of this article).

constant k of CW-0.80 is 68 μmol g^{-1} h^{-1} almost as 45.3 times as that of pure g-C$_3$N$_4$ (1.5 μmol g^{-1} h^{-1}). As shown in Fig. S2a, in ten consecutive reactions, the H$_2$ evolution increases steadily as the irradiation time increases with no difference. The other CW photocatalysts show lower H$_2$ production than CW-0.80 in varying degrees under full-spectrum light irradiation (Fig. S2b).

The differences of g-C$_3$N$_4$, Cs$_x$WO$_3$ and CW were further confirmed by the photocatalytic degradation of RhB under full-spectrum light irradiation. As can be seen in Fig. 2d, a first-order linear relationship is revealed by the plots of ln(C/C_0) versus irradiation time, and the value of the rate constant k is equal to the corresponding slope of the fitting line. All of the CW photocatalysts exhibit much higher photocatalytic degradation activity than pure Cs$_x$WO$_3$ under light irradiation. The increase of g-C$_3$N$_4$ proportion results in the gradual improvement of the photocatalytic activity. CW-0.80 with 80% of g-C$_3$N$_4$ has a higher photocatalytic activity than g-C$_3$N$_4$. The determined rate constant k is 2.47 h^{-1} almost as 1.4 times as that of pure g-C$_3$N$_4$ (1.80 h^{-1}) and 12.4 times pure Cs$_x$WO$_3$ (0.20 h^{-1}). However, no more enhancement of photocatalytic activity is observed between CW-0.80 and CW-0.83. It is notable that the mechanical blend does not obviously enhance the photocatalytic activity, implying that there may be some interaction between g-C$_3$N$_4$ and Cs$_x$WO$_3$ that plays an important role in improving the photocatalytic activity.

When using red LED lamp with the wavelength of 660 nm as the light source, CW-0.80 also exhibits good photocatalytic H$_2$ evolution ability (in Fig. S2c). CW-0.80 can produce 1510 μmol/g of H$_2$ in 5 h

under red light irradiation with the wavelength of 660 nm, while pure Cs$_x$WO$_3$ and g-C$_3$N$_4$ show no activity. CW-0.80 also exhibits better photocatalytic ability of RhB degradation than pure Cs$_x$WO$_3$ and g-C$_3$N$_4$ under red light irradiation (in Fig. S2d).

To investigate the active species involved in the photocatalytic reaction process, the evaluation was carried out by adding different active radical captures in the RhB solution over CW-0.80 under different light source irradiation. The experimental results compared with no addition one is shown in Fig. 2e.

By inducing ·O^{2-} and ·OH scavenger into system, BQ and IPA, CW-0.80 exhibits a significant decrease in the UV light photocatalytic activity owing to the less active species to drive the reaction (Fig. 2e2). Conversely, the photocatalytic performance hardly changes by adding holes scavenger, AO. This results imply that both ·O^{2-} and ·OH generated on CW-0.80 play an important role in RhB decomposition and the ·O^{2-} radicals are the main oxidative species under UV light irradiation.

However, under visible light (blue or red light) irradiation, the addition of one of BQ, IPA, or AO causes the decrease of photocatalytic activity over CW-0.80 (in Fig. 2e3–e4). All of the ·O^{2-}, ·OH and h^+ are crucial to RhB degradation under visible light irradiation. The ·O^{2-} radicals are the main oxidative species under blue light irradiation and the h^+ radicals are the key point under red light irradiation. In
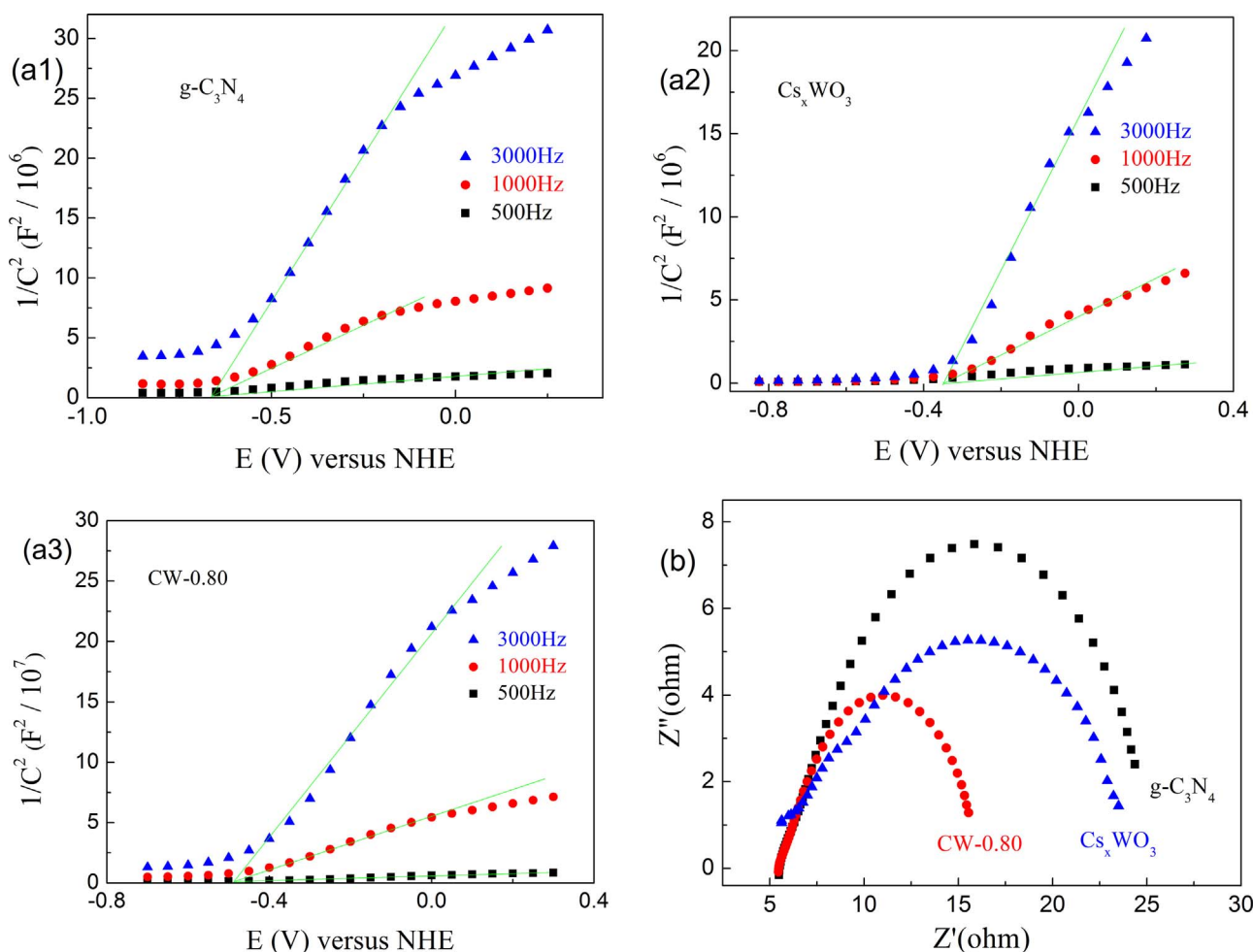
Fig. 6. Mott-Schottky plots of (a1) g-C$_3$N$_4$, (a2) Cs$_x$WO$_3$ and (a3) CW-0.80; (b) Nyquist impedance plots for g-C$_3$N$_4$, Cs$_x$WO$_3$ and CW-0.80.

addition, as shown in Fig. 2e1, for full spectrum driven photocatalytic degradation, all theses radicals are important and the ·O^{2-} radicals are the most important one. For more details, see the Fig. S3a-d.

To further verify the existence of ·O^{2-} radicals directly, EPR measurement was carried out. Fig. 2f shows four different EPR spectra of O$_2$·$^-$ generated from CW-0.80 under different light irradiation compared with that without light irradiation. The strong signals are ascribed to the nitroxide-like radical which may be formed by the light-induced decomposition of the unstable DMPO-O$_2$·$^-$ adduct [43]. It can be clear seen that the intensity of DMPO-O$_2$·$^-$ signals decreases as the irradiation light gets longer wavelength. After red light irradiation, the DMPO-O$_2$·$^-$ signals are too weak to be observed. The results reveal again that O$_2$·$^-$ radicals are not the main oxidative species under red light irradiation. However, under short wavelength light irradiation especially UV light, O$_2$·$^-$ can be produced.

3.3. Generation of photocatalytic degradation and H$_2$ evolution in NIR region

The NIR light induced photocatalytic activity of CW-0.80 was determined for both the H$_2$ evolution and the degradation of RhB. For comparison, g-C$_3$N$_4$ and Cs$_x$WO$_3$ were used as a photocatalytic references under the same experimental conditions. In Fig. 3a and b, the results highlights that g-C$_3$N$_4$ exhibits no catalytic activity under NIR light (980 nm) irradiation. Only a negligible amount of the RhB is degraded over Cs$_x$WO$_3$ but no H$_2$ is obtained. However, CW-0.80 can not only split water for H$_2$ evolution but also degrade RhB. In Fig. 3a, the CW-0.80 photocatalyst could make 50 μmol/g of H$_2$ after 5 h

photocatalytic reaction with NIR light irradiation. As shown in Fig. 3b, under NIR light irradiation, the *k* of CW-0.80 is 6.6 × 10^{-3} h^{-1} almost as 1.7 times as that of pure Cs$_x$WO$_3$ (3.92 × 10^{-3} h^{-1}). When NIR laser with 808 nm is used as light source, CW-0.80 also exhibits higher photocatalytic activity than Cs$_x$WO$_3$ though their *k* values are higher than those under laser irradiation with the wavelength of 980 nm (in Fig. S4a and b).

The active species were determined by using NIR light source. As shown in Fig. 3c, in the CW-0.80 system under a 500 mW laser irradiation (980 nm), the addition of a scavenger of ·O^{2-} radicals (BQ) only caused a small change in the photodegradation of RhB. On the contrary, the photocatalytic activity of CW-0.80 could be greatly suppressed by the addition of a scavenger for ·OH (IPA) or *h*$^+$ (AO). This result suggests that the photogenerated holes are the main oxidative species of the CW-0.80 under NIR light irradiation. It can be confirmed that the ·O^{2-} radicals are not the main oxidative species since the DMPO-·O^{2-} signals are too weak to be observed after NIR light irradiation (in Fig. 3d).

Therefore, the CW-0.80 heterostructure exhibits an enhanced degradation rate and H$_2$ evolution efficiency under UV–vis and NIR light irradiation.

3.4. Photoelectrochemical and electrochemical activities in visible light region

CW-0.80, g-C$_3$N$_4$ and Cs$_x$WO$_3$ were selected for studying the PEC/EC degradation of phenol. The PC degradation was carried out over the same photocatalyst electrode. Since a white LED lamp (400–750 nm)
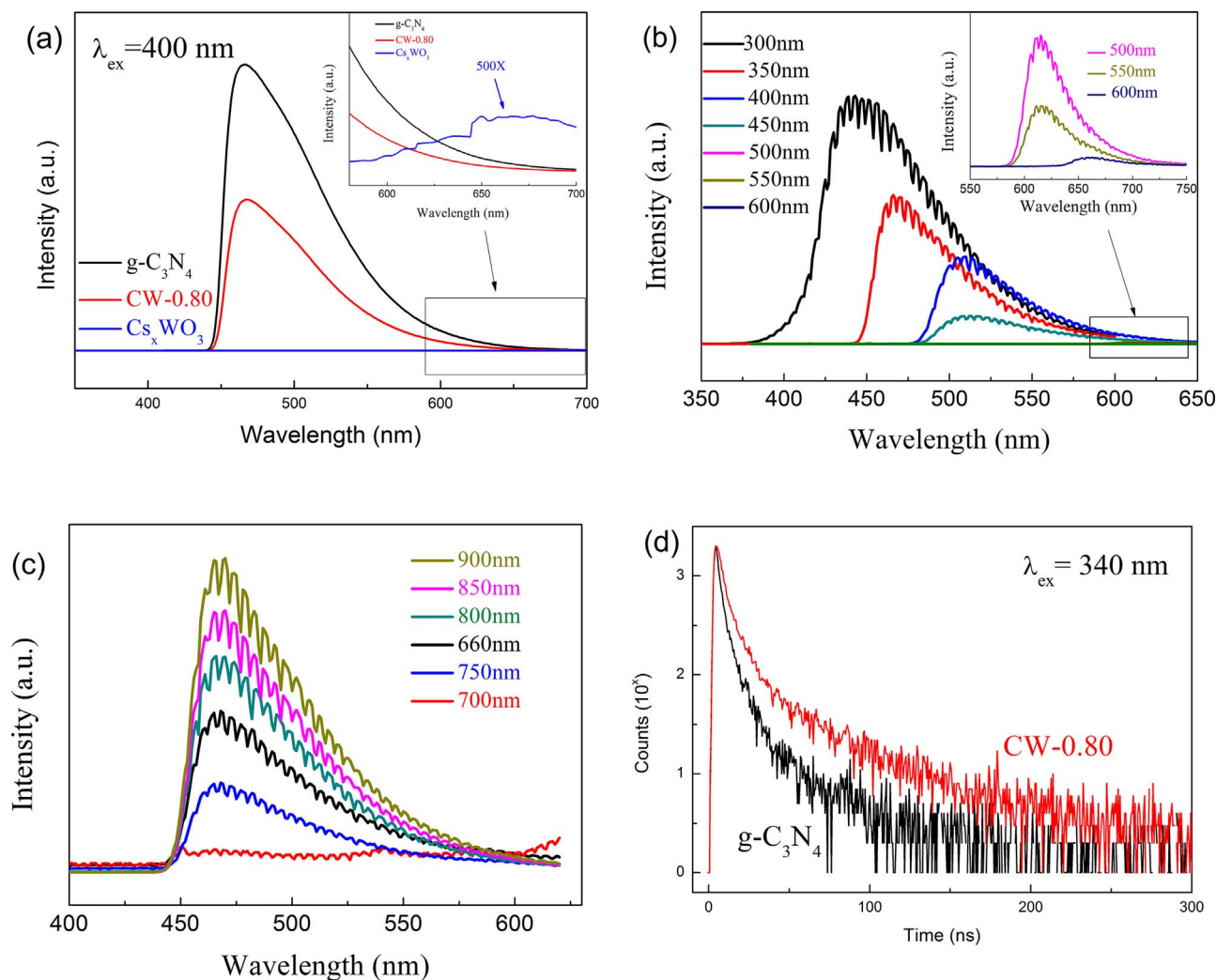
Fig. 7. (a) PL spectra of g-C$_3$N$_4$, Cs$_x$WO$_3$ and CW-0.80; (b) down-converted and (c) up-converted PL spectra of CW-0.80; (d) time-resolved PL spectra monitored at 450 nm of g-C$_3$N$_4$ and CW-0.80. (For interpretation of the references to colour in text, the reader is referred to the web version of this article).

with the intensity of 9.4 mW/cm^2 was used as light source, the photocatalyst electrode with an area of 1.5 cm^2 shows not high activity. Even so, the difference among CW-0.80, g-C$_3$N$_4$ and Cs$_x$WO$_3$ could be well investigated.

Fig. 4a shows the EC, PC and PEC degradation efficiency of phenol in 5 h. As can be seen from the rate constant values (k) of CW-0.80, g-C$_3$N$_4$ and Cs$_x$WO$_3$, CW-0.80 is more efficient than pure g-C$_3$N$_4$ and Cs$_x$WO$_3$ on all phenol degradation. When the degradation reaction was proceeding over CW-0.80, the EC degradation k of phenol reached $23.7 \times 10^{-3}\,h^{-1}$. The k values of g-C$_3N_4$ and Cs$_x$WO$_3$ are 17.2×10^{-3} and $15.8 \times 10^{-3}\,h^{-1}$ respectively. For PC degradation with visible light irradiation, CW-0.80 is also more active than pure g-C$_3$N$_4$ and Cs$_x$WO$_3$. CW-0.80 shows a higher k value of $29.1 \times 10^{-3}\,h^{-1}$ than $18.7 \times 10^{-3}\,h^{-1}$ of g-C$_3$N$_4$ and $2.84 \times 10^{-3}\,h^{-1}$ of Cs$_x$WO$_3$. The composition can increase the free charge carriers, which results from the promoted separation [44]. As g-C$_3$N$_4$ and Cs$_x$WO$_3$ coupled, the free electrons increased, and hence the EC/PC degradation efficiency of phenol increased, compared with pure g-C$_3$N$_4$ and Cs$_x$WO$_3$. Compared with EC degradation efficiency, all photocatalyst electrodes show little higher activity in PC degradation with visible light irradiation. The limited EC/PC degradation efficiency is due to the limited electrode area and the weak irradiation intensity. For more details, see the Fig. S5a–c.

The EC degradation efficiency of phenol is greatly increased by the visible light, which is the PEC degradation (Fig. 4a). CW-0.80 exhibits a dramatic increase of PEC degradation ability, while those of g-C$_3$N$_4$ and Cs$_x$WO$_3$ also increase to some degree. It is note worthy that the rate constant of CW-0.80 is much larger than the sum of that of pure g-C$_3$N$_4$ and Cs$_x$WO$_3$. It suggests that the interaction between g-C$_3$N$_4$ and Cs$_x$WO$_3$ can significantly enhance the activity of CW composite. The PEC activity of CW-0.80 ($152.7 \times 10^{-3}\,h^{-1}$) under visible light irradiation is almost 2.2 times as high as that of g-C$_3$N$_4$ ($70.0 \times 10^{-3}\,h^{-1}$) and 4.1 times of Cs$_xWO_3$ ($37.1 \times 10^{-3}\,h^{-1}$).

Photocurrents were measured for CW-0.80, g-C$_3$N$_4$ and Cs$_x$WO$_3$ electrodes to investigate the electronic interaction between g-C$_3$N$_4$ and Cs$_x$WO$_3$ in CW-0.80 under visible light irradiation (Fig. 4b). All electrodes show uniform and reversible photocurrent responses. Under visible light irradiation, the photocurrent of the CW-0.80 electrode is about 4.2 times as high as that of the pure g-C$_3$N$_4$ electrode and 2.2 times Cs$_x$WO$_3$. The improved photocurrent of CW-0.80 reveals that an enhanced photoinduced electrons and holes separation, which could be attributed to the synergetic effect of g-C$_3$N$_4$ and Cs$_x$WO$_3$.

3.5. Mechanistic studies

To clarify the catalytic essence of as-prepared photocatalysts, more measurements were carried out to investigate the difference among g-C$_3$N$_4$, Cs$_x$WO$_3$ and CW.

First, to exclude the effect of surface area on the catalytic efficiency, the specific surface area of g-C$_3$N$_4$, Cs$_x$WO$_3$ and CW-0.80 was
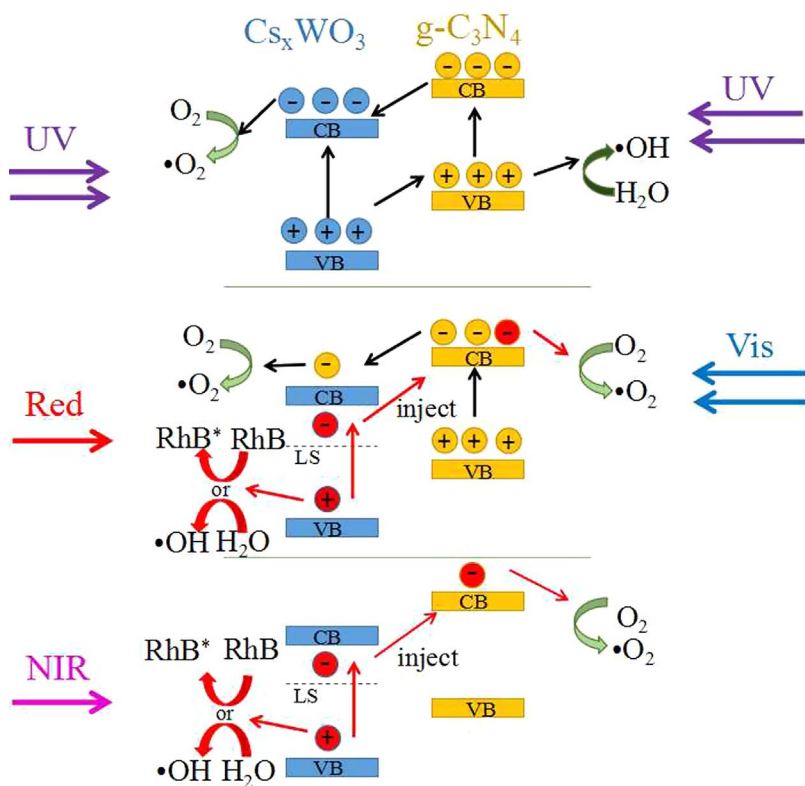
Fig. 8. Schematic photocatalytic mechanism for the CW-0.80 composite under UV–vis and NIR light irradiation. (LS: localized state). (For interpretation of the references to colour in text, the reader is referred to the web version of this article).

evaluated. The BET specific surface area of CW-0.80 is 35.7 m²/g, while that is 37.6 m²/g for g-C_3N_4 and 32.5 m²/g for Cs_xWO_3 (Table 1). In addition, the average particle sizes of the as-prepared samples were determined by DLS. As shown in Table 1, CW-0.80 has an average particle size of 332 nm, while 308 nm of g-C_3N_4 and 177 nm of Cs_xWO_3. Since there are no significant changes in the BET surface area among pure g-C_3N_4, Cs_xWO_3 and CW-0.80, indicating that surface area is not crucial for inducing the difference in catalytic ability. The significant enhancement of catalytic activity is mainly due to the improved charge transfer.

DRS spectra were measured to evaluate the optical absorption ability of g-C_3N_4, Cs_xWO_3 and CW-0.80 and shown in the insert of Fig. 5a. For pure g-C_3N_4, the strongest absorption occurs at about 365 nm, consistent with the band gap of protonated single layer g-C_3N_4, [45–47] while the absorption intensity of pure Cs_xWO_3 increases rapidly from red light to NIR region, in good accordance with its LSPR effect [21–24]. Thanks to the coexistence of g-C_3N_4 and Cs_xWO_3, CW-0.80 can absorb not only UV light but also visible light and even NIR light. In Fig. S6, all the CW composites show a broad range of absorption from UV, Vis to NIR region. According to the Kubelka-Munk relation, the band gaps are calculated at 2.96, 3.21 and 2.98 eV for g-C_3N_4, Cs_xWO_3 and CW-0.80 respectively (Fig. 5a). Then, the relative valence band maximum was determined via valence band XPS measurement, as shown in Fig. 5b. Therefore, the conduction band (CB) edges and valence band (VB) edges of g-C_3N_4, Cs_xWO_3 and CW-0.80 are calculated at −0.76, −0.25, −0.54 and 2.20, 2.96, 2.44 eV, respectively.

As shown in Mott-Schottky plots (Fig. 6a), the flat-band potentials are determined to be −0.66, −0.35 and −0.49 V for g-C_3N_4, Cs_xWO_3 and CW-0.80 respectively. All samples should be of n-type characteristics owing to the positive slopes of the linear plots. In the electrochemical impedance spectroscopy (EIS) evaluation (Fig. 6b), according to the semicircle in the low-frequency zone, the charge transfer resistances of g-C_3N_4, Cs_xWO_3 and CW-0.80 are calculated to be 27.4, 24.6 and 10.8 Ω, indicating that CW-0.80 has a faster charge transfer rate. In addition, whatever the irradiation source (460, 660 or 980 nm

light), the CW-0.80 exhibits excellent charge transfer rate (in Fig. S7).

Next, PL analysis was used to further analyze the recombination rate of photo-generated carriers. As shown in Fig. 7 a, pure g-C_3N_4 exhibit the strongest photoluminescence with an emission peak at about 466 nm, owing to the band-band PL phenomenon. Compared with pure ones, the PL intensity of CW-0.80 is much weaker, suggesting a slower recombination of electrons and holes. The PL intensities of other CW composites are lower than that of CW-0.80 in different degrees except CW-0.83 and all of them are much weaker than that of pure g-C_3N_4 (Fig. S8a), while that of Cs_xWO_3 is too weak. As shown in Fig. S8b, with the excitation wavelength increases from 400 to 600 nm, the PL intensity of Cs_xWO_3 decreases according to the fewer excited electrons. Its emission peaks are located at ca. 675 nm.

To further explore the optical properties of CW-0.80, PL was studied using different excitation wavelengths (Fig. 7b and c). Fig. 7b shows the down-converted PL spectra of CW-0.80 within the excitation range of 300–600 nm. When the excitation wavelength changes from 300 to 600 nm, the PL peak correspondingly shifts from 440 (blue) to 660 nm (red). Under the excitation with a wavelength of 300 nm, CW-0.80 appears the most intense PL at 440 nm. Fig. 7c shows the up-converted PL spectra of CW-0.80 under the excitation with the wavelength from 660 to 900 nm. Whatever the excitation, the emissions are located at visible light region of 443–600 nm. The result reveals that CW-0.80 can be excited by UV, visible and NIR light to produce electrons and holes.

The PL decay was studied by time-resolved spectra. As can be seen in Fig. 7d, CW-0.80 has a longer lifetime than g-C_3N_4, indicating a slower charge recombination. Since the decay curves are fitted to the one-exponential function, the average lifetimes of the entire decay are calculated to be 9.32 and 15.92 ns for g-C_3N_4 and CW-0.80 respectively. The photogenerated charge carrier behaviors were investigated by TAS. In addition, CW-0.80 exhibit much more persistent transient signal than g-C_3N_4 in TAS (Fig. S9). It indicates that CW-0.80 has a relatively long lived charge separation state which will be benefit for catalytic reactions.

Combined with the above results, a schematic for electron–hole separation and transportation at the g-C_3N_4/Cs_xWO_3 photocatalyst is

shown in Fig. 8.

First, intramolecular charge transfer will take place under irradiation which results in the effective separation of charge carriers in the conjugated donor-acceptor g-C$_3$N$_4$ [48–50].

Both Cs$_x$WO$_3$ and g-C$_3$N$_4$ can be excited by UV light to produce electron–hole pairs. Since the VB potential of Cs$_x$WO$_3$ is higher than g-C$_3$N$_4$, the photogenerated holes on Cs$_x$WO$_3$ could directly transfer to g-C$_3$N$_4$. On the other hand, the photogenerated electrons in g-C$_3$N$_4$ can easily transfer to Cs$_x$WO$_3$ since the CB potential of g-C$_3$N$_4$ is lower than Cs$_x$WO$_3$. The transfer of holes and electrons in the hybrid heterojunction structure can promote charge separation and reduce the recombination probability, resulting in an enhanced photocatalytic activity. The $\cdot$O^{2-} radicals are the main oxidative species for photocatalysis reactions under UV light irradiation.

As shown in Fig. 8, under visible light irradiation, the π–π* transition will occur in g-C$_3$N$_4$ to induce the excited-state electrons transition from the HOMO to the LUMO [2,51,52]. Then, the excited electron in g-C$_3$N$_4$ can easily transfer to Cs$_x$WO$_3$ since their proper band structures. After lost electron, g-C$_3$N$_4$$^+$ will seize electrons from water splitting or RhB degradation back to the ground state. Superoxide and hydroxyl radicals will be produced during these electrons subsequently transfer to the surface of photocatalyst. The charge carriers' separation is highly enhanced under visible light irradiation, compared with that under UV light irradiation. When the irradiation wavelength rises up to red light region, the LSPR is induced in the Cs$_x$WO$_3$. According to the LSPR effect, the hot electrons transferred from Cs$_x$WO$_3$ to g-C$_3$N$_4$ will significantly increase the number of photoinduced electrons for highly efficient photochemical processes. The $\cdot$O^{2-} radicals are still the key oxidative species for photocatalysis reactions under visible light irradiation and the importance of h^+ should not be ignored.

Under NIR light irradiation, with the LSPR effect, the hot electrons will be injected into the CB of g-C$_3$N$_4$, and the holes left behind in the Cs$_x$WO$_3$ where oxidation reactions take place, similar to plasmonic metal/semiconductor hybrids (Fig. 8) [16,48]. In addition, the localized oscillating electric field induced by the LSPR effect will promote the charge separation and lower the H$_2$-over potential [48,53]. The enhanced electric field is localized close to the interface, reducing the probability of charge-carrier recombination in the photocatalyst. The h^+ radicals are crucial for photocatalysis reactions under NIR light irradiation. On the basis of the above results and analyses, it reveals that the coupling of Cs$_x$WO$_3$ and g-C$_3$N$_4$ is the optimal synergistic effect among the heterostructure composites for achieving highly efficient catalytic ability.

To further investigate the stability of CW-0.80 composite, some characterizations about CW-0.80 sample were also carried out before and after 10 times photocatalytic cycle reaction. As shown in Fig. S10a-c, these two CW-0.80 samples, fresh and used one, do not have any difference in XRD, FTIR, and UV-vis DRS results. The new CW-0.80 shows a large particle size with an average particle size of 332 nm (d$_{50}$), while that of the one after photocatalytic reaction is 355 nm (d$_{50}$) (Fig. S10d). The similar average particle size suggests that the composite is stable in photocatalytic process. In addition, TEM image of the CW-0.80 after photocatalytic reaction is the same as that of fresh one (Fig. S10e and Fig. 1a). Therefore, no obvious change confirms the high stability of CW-0.80 in the photocatalytic process.

4. Conclusion

In summary, g-C$_3$N$_4$/Cs$_x$WO$_3$ composite has been fabricated successfully by a simple method. After evaluated the photocatalytic and photoelectrochemical activity for H$_2$ evolution and RhB/phenol degradation under UV, visible and NIR light irradiation, it shows that the composite could efficiently harvest different light to boost the charge transfer and electron-hole separation. Comparison investigations reveal that with the LSPR effect and heterostructure effect, the g-C$_3$N$_4$/Cs$_x$WO$_3$ composite exhibits synergistically improved catalytic activity

for H$_2$ evolution and RhB/phenol degradation. Since the good charge separation efficiency and quick surface kinetics in full-spectrum light region, it is anticipated that this strategy would provide an optimal choice to enhance the solar energy utilization.

Appendix A. Supplementary data

Supplementary material related to this article can be found, in the online version, at doi:https://doi.org/10.1016/j.apcatb.2018.01.070.

References

[1] Y. Zheng, L. Lin, B. Wang, X. Wang, Angew. Chem. Int. Ed. 54 (2015) 12868–12884.
[2] Y. Wang, R. Shi, J. Lin, Y. Zhu, Energy Environ. Sci. 4 (2011) 2922–2929.
[3] S.P. Adhikari, Z.D. Hood, H. Wang, R. Peng, A. Krall, H. Li, V.W. Chen, K.L. More, Z. Wu, S. Geyer, A. Lachgar, Appl. Catal. B Environ. 217 (2017) 448–458.
[4] W. Wang, T. An, G. Li, D. Xia, H. Zhao, J.C. Yue, P.K. Wong, Appl. Catal. B Environ. 217 (2017) 570–580.
[5] J. Ma, X. Tan, F. Jiang, T. Yu, Catal. Sci. Technol. 7 (2017) 3275–3282.
[6] Y. Hong, Z. Fang, B. Yin, B. Luo, Y. Zhao, W. Shi, C. Li, Int. J. Hydrogen. Energy 42 (2017) 6738–6745.
[7] L. Yao, L. Wei, Y. Ni, D. Yan, C. Hu, Nano Energy 26 (2016) 248–256.
[8] X. Zhang, Z. Meng, D. Rao, Y. Wang, Q. Shi, Y. Liu, H. Wu, K. Deng, H. Liu, R. Lu, Energy Environ. Sci. 9 (2016) 841–849.
[9] H. Li, X. Wu, S. Yin, K. Katsumata, Y. Wang, Appl. Surf. Sci. 392 (2017) 531–539.
[10] D.J. Martin, P.J.T. Reardon, S.J.A. Moniz, J. Tang, J. Am. Chem. Soc. 136 (2014) 12568–12571.
[11] S. Ma, K. Maeda, R. Abe, K. Domen, Energy Environ. Sci. 5 (2012) 8390–8397.
[12] B. Li, X. Shao, T. Liu, L. Shao, B.Z. School, Appl. Catalysis B Environ. 198 (2016) 325–333.
[13] H. Takeda, K. Adachi, J. Am. Ceram. Soc. 90 (2007) 4059–4061.
[14] K. Manthiram, A.P. Alivisatos, J. Am. Chem. Soc. 134 (2012) 3995–3998.
[15] J. Chen, D. Yu, W. Liao, M. Zheng, L. Xiao, H. Zhu, M. Zhang, M. Du, J. Yao, ACS Appl. Mater. Interfaces 8 (2016) 18132–18139.
[16] O. Elbanna, S. Kim, M. Fujitsuka, T. Majima, Nano Energy 35 (2017) 1–8.
[17] B. Wu, W. Liu, T. Chen, T. Perng, J. Huang, L. Chen, Nano Energy 27 (2016) 412–419.
[18] J. Yan, T. Wang, G. Wu, W. Dai, N. Guan, L. Li, J. Gong, Adv. Mater. 27 (2015) 1580–1586.
[19] J. Liu, O. Margeat, W. Dachraoui, X. Liu, M. Fahlman, J. Ackermann, Adv. Funct. Mater. 24 (2014) 6029–6037.
[20] Z. Zhang, J. Huang, Y. Fang, M. Zhang, K. Liu, B. Dong, 1606688, Adv. Mater. 29 (2017).
[21] W. Guo, C. Guo, N. Zheng, T. Sun, S. Liu, 1604157, Adv. Mater. 29 (2017).
[22] T.M. Mattox, A. Bergerud, A. Agrawal, D.J. Milliron, Chem. Mater. 26 (2014) 1779–1784.
[23] G. Li, C. Guo, M. Yan, S. Liu, Appl. Catal. B Environ. 183 (2016) 142–148.
[24] K. Machida, K. Adachi, J. Phys. Chem. C 120 (2016) 16919–16930.
[25] C. Ye, J. Li, Z. Li, X. Li, X. Fan, L. Zhang, B. Chen, C. Tung, L. Wu, ACS Catal. 5 (2015) 6973–6979.
[26] X. She, J. Wu, J. Zhong, H. Xu, Y. Yang, R. Vajtai, J. Lou, Y. Liu, D. Du, H. Li, P. Ajayan, Nano Energy 27 (2016) 138–146.
[27] J. Choi, K. Moon, I. Kang, S. Kim, P.J. Yoo, K.W. Oh, J. Park, Chem. Eng. J. 281 (2015) 236–242.
[28] L.H.M. Krings, W. Talen, Sol. Energy Mater. Sol. Cells 54 (1998) 27–37.
[29] A.K.L. Sajjad, S. Shamaila, J. Zhang, Mater. Res. Bull. 47 (2012) 3083–3089.
[30] X. Chen, C. Burda, J. Phys. Chem. B 108 (2004) 15446–15449.
[31] S. Sakthivel, M. Janczarek, H. Kisch, J. Phys. Chem. B 108 (2004) 19384–19387.
[32] R. Asahi, T. Morikawa, T. Ohwaki, K. Aoki, Y. Taga, Science 293 (2001) 269–271.
[33] H.X. Li, J.X. Li, Y. Huo, J. Phys. Chem. B 110 (2006) 1559–1565.
[34] G. Sauthier, E. György, A. Figueras, R.S. Sánchez, J. Hernando, J. Phys. Chem. C 116 (2012) 14534–14540.
[35] J. Yan, T. Wang, G. Wu, W. Dai, N. Guan, L. Li, J. Gong, Adv. Mater. 27 (2015) 1580–1586.
[36] C. Zhou, C. Lai, D. Huang, G. Zeng, C. Zhang, M. Cheng, L. Hu, J. Wan, W. Xiong, M. Wen, X. Wen, L. Qin, Appl. Catal. B Environ. 220 (2018) 202–210.
[37] F. Dong, Y. Li, Z. Wang, W.-K. Ho, Appl. Surf. Sci. 358 (2015) 393–403.
[38] C. Dong, Z. Ma, R. Qie, X. Guo, C. Li, R. Wang, Y. Shi, B. Dai, X. Jia, Appl. Catal. B Environ. 217 (2017) 629–636.

[39] L. Gao, T. Wen, J. Xu, X. Zhai, M. Zhao, G. Hu, P. Chen, Q. Wang, H. Zhang, ACS Appl. Mater. Interfaces 8 (2016) 617–624.
[40] W. Yang, X. Zhang, Y. Xie, Nano Today 11 (2016) 793–816.
[41] Y. Li, Z. Wang, T. Xia, H. Ju, K. Zhang, R. Long, Q. Xu, C. Wang, L. Song, J. Zhu, J. Jiang, Y. Xiong, Adv. Mater. 28 (2016) 6959–6965.
[42] Z. Xi, D.P. Erdosy, A.M. Garcia, P.N. Duchesne, J. Li, M. Muzzio, Q. Li, P. Zhang, S. Sun, Nano Lett. 17 (2017) 2727–2731.
[43] C. Uribe, M. Daza, F. Martinez, E. Mozo, C. Guedes, E. Mauro, J. Photochem. Photobiol. A Chem. 215 (2010) 172–178.
[44] Z. Wei, F. Liang, Y. Liu, W. Luo, J. Wang, W. Yao, Y. Zhu, Appl. Catal. B Environ. 201 (2017) 600–606.
[45] J. Xu, L. Zhang, R. Shi, Y. Zhu, J. Mater. Chem. A 1 (2013) 14766–14772.
[46] X. Zhang, H. Wang, H. Wang, Q. Zhang, J. Xie, Y. Tian, J. Wang, Y. Xie, Adv. Mater. 26 (2014) 4438–4443.
[47] X. Zhang, X. Xie, H. Wang, J. Zhang, B. Pan, Y. Xie, J. Am. Chem. Soc. 135 (2013) 18–21.
[48] X. Wei, C. Shao, X. Li, N. Lu, K. Wang, Z. Zhang, Y. Liu, Nanoscale 8 (2016) 11034–11043.
[49] X. Chen, Q. Liu, Q. Wu, P. Du, J. Zhu, S. Dai, S. Yang, Adv. Funct. Mater. 26 (2016) 1719–1728.
[50] X. Fan, L. Zhang, R. Cheng, M. Wang, M. Li, Y. Zhou, J. Shi, ACS Catal. 5 (2015) 5008–5015.
[51] Y. Zhang, J. Liu, J. Liang, M. Jaroniecc, S.Z. Qiao, Energy Environ. Sci. 5 (2012) 6717–6731.
[52] F. Wang, P. Chen, Y. Feng, Z. Xie, Y. Liu, Y. Su, Q. Zhang, Y. Wang, K. Yao, W. Lv, G. Liu, Appl. Catal. B Environ. 207 (2017) 103–113.
[53] X. She, J. Wu, H. Xu, Z. Mo, J. Lian, Y. Song, L. Liu, D. Du, H. Li, Appl. Catal. B Environ. 202 (2017) 112–117.